ANNUAL REVIEWS

Annual Review of Biochemistry

High-Resolution Single-Molecule Magnetic Tweezers

Hyun-Kyu Choi,[1,*] Hyun Gyu Kim,[2,*] Min Ju Shon,[3] and Tae-Young Yoon[2]

[1]Wallace H. Coulter Department of Biomedical Engineering and Parker H. Petit Institute for Bioengineering and Bioscience, Georgia Institute of Technology, Atlanta, Georgia, USA

[2]School of Biological Sciences and Institute for Molecular Biology and Genetics, Seoul National University, Seoul, South Korea; email: tyyoon@snu.ac.kr

[3]Department of Physics and School of Interdisciplinary Bioscience and Bioengineering, Pohang University of Science & Technology (POSTECH), Pohang, South Korea; email: mjshon@postech.ac.kr

Annu. Rev. Biochem. 2022. 91:33–59

First published as a Review in Advance on March 14, 2022

The *Annual Review of Biochemistry* is online at biochem.annualreviews.org

https://doi.org/10.1146/annurev-biochem-032620-104637

*These authors contributed equally to this article

Keywords

magnetic tweezers, high-resolution magnetic tweezers, single molecules, single-molecule force spectroscopy, mechanotransduction, protein folding

Abstract

Single-molecule magnetic tweezers deliver magnetic force and torque to single target molecules, permitting the study of dynamic changes in biomolecular structures and their interactions. Because the magnetic tweezer setups can generate magnetic fields that vary slowly over tens of millimeters—far larger than the nanometer scale of the single molecule events being observed—this technique can maintain essentially constant force levels during biochemical experiments while generating a biologically meaningful force on the order of 1–100 pN. When using bead–tether constructs to pull on single molecules, smaller magnetic beads and shorter submicrometer tethers improve dynamic response times and measurement precision. In addition, employing high-speed cameras, stronger light sources, and a graphics programming unit permits true high-resolution single-molecule magnetic tweezers that can track nanometer changes in target molecules on a millisecond or even submillisecond time scale. The unique force-clamping capacity of the magnetic tweezer technique provides a way to conduct measurements under near-equilibrium conditions and directly map the energy landscapes underlying various molecular phenomena. High-resolution single-molecule magnetic tweezers

can thus be used to monitor crucial conformational changes in single-protein molecules, including those involved in mechanotransduction and protein folding.

Contents

1. INTRODUCTION

Most living organisms exhibit minimal magnetic properties, making them largely insensitive to external magnetic fields. The introduction of exogenous magnetic material (e.g., iron oxide particles) opens a host of possibilities for the selective modulation of these particles as part of our efforts to better understand complex biological phenomena. The use of magnetism in the biological sciences stretches back to Freundlich and Seifriz, who first introduced nickel particles into gelatin a century ago (1). It then took a few more decades for the concept to be picked up again by Crick and Hughes (2). Their experiments moving phagocytosed magnetic particles with a magnet in an effort to study the physical properties of chick fibroblast cytoplasm were arguably the first scientific protocol for a magnetic particle method.

Over the past two decades, scientific protocols for applying magnetic forces to biological samples have matured to the point where individual biomolecules can be monitored and controlled in real time. The first demonstration of the magnetic movement of single DNA molecules (3) was pioneering work that culminated in the techniques we collectively refer to today as magnetic tweezers (4–7), now regarded as a principal form of single-molecule force spectroscopy alongside optical tweezers (8–12) and atomic force microscopy (AFM) (13–16). These single-molecule tweezer techniques have proven extremely useful for reductionist systems in which key biological processes are reconstituted outside cells so their behaviors under different levels of molecular tension can be investigated in unprecedented detail (17). Single-molecule force spectroscopy has been used to address a wide range of phenomena, including the mechanics of biopolymers (3–6, 10, 15, 18–23), the dynamics of motor proteins (8, 9, 24–28), the pathways of protein folding and unfolding (14, 16, 29–34), ligand–receptor binding (13, 35–37), and more recently, the association and dissociation of biomolecular complexes involved in mechanobiological processes (38–42).

The three main techniques of single-molecule force spectroscopy have coevolved, sharing many technological advances while also each developing its own technical niche (17). The

resolution and precision of the optical tweezer technique invented by Arthur Ashkin and colleagues in 1986 (43) have improved to the point where molecular events can be dissected at the level of individual DNA base pairs (27, 44). Optical tweezer techniques are limited because the intense laser illuminations they require can cause heat-mediated sample destruction (45) and optical scattering makes it impossible to probe the deeper layers of biological samples (46–48). AFM was first developed for use in surface imaging and has been extended to the pulling of single molecules attached to the ends of AFM cantilevers (49). Structural changes in the attached molecules are coupled to the cantilever, which is monitored by high-bandwidth measurements limited only by the readout electronics being employed (33, 50). Despite recent advances providing a few notable exceptions (50–53), the size and stiffness of the cantilever probes have largely limited their application to relatively large force regimes spanning hundreds of piconewtons or even higher (17).

Magnetic tweezers pull magnetic particles by generating magnetic field gradients across space (54, 55). The magnetic particles and their attached molecules are monotonically attracted toward the space surrounding magnets where the field gradients are most steeply changing. Target molecules are usually tethered to a nearby surface to create a mechanical equilibrium between the magnetic pulling force and the elastic restoring force from the tether (56). In the optical tweezer and AFM techniques, the force levels change sharply over the length of focused gaussian beams and AFM cantilever tips (17). The magnetic tweezer technique, in contrast, forms largely uniform field vectors using multiple magnets, permitting the formation of field vector gradients that change appreciably only on a millimeter scale. This means that the nanometer-scale changes that accompany biological processes do not affect the magnetic force experienced by the magnetic particles, completely decoupling the biological processes in question and the magnetic tweezing. Thus, many magnetic tweezer experiments can be conducted in an inherent force-clamp mode, in which the target molecules are modulated and monitored under essentially constant force.

Magnetic tweezer setups rely on image analysis to track the three-dimensional position of the magnetic particles, a critical limitation in increasing measurement bandwidth (57). Most earlier applications of the magnetic tweezer technique had to contend with the large-scale conformational changes in nucleic acids that occur under quasi-equilibrium conditions (3, 4, 10). Recently, technical advancements toward higher-resolution magnetic tweezers have permitted the monitoring of nanoscale (or even subnanoscale) changes in target molecules with higher temporal resolutions (sometimes reaching the submillisecond scale) (57–59). In this review, we discuss the physical principles and limitations guiding the development of high-resolution magnetic tweezers. In addition, because many biological processes are regulated by mechanical tension (60, 61), we discuss how high-resolution magnetic tweezers have been used to answer fundamental questions in mechanobiology, protein biogenesis, and homeostasis. To promote the application of these techniques to problems in a wide range of fields, we conclude this review by offering an outlook for the future of single-molecule magnetic tweezers.

2. PRINCIPLES OF MAGNETIC PULLING

2.1. Pulling with Biologically Meaningful Force

Most biomolecules range in size from the subnanometer scale to tens of nanometers, with physical dimensions that are significantly influenced by Brownian noise (62). The structures of biological molecules and the interactions between them are stabilized by energy scales larger than those of thermal fluctuations (represented as $\sim 1\ k_B T$, where k_B is the Boltzmann constant and T is the absolute temperature) (63). At the same time, the free energy values of these interactions are smaller than those of covalent bonds, which typically span hundreds of $k_B T$. This means the

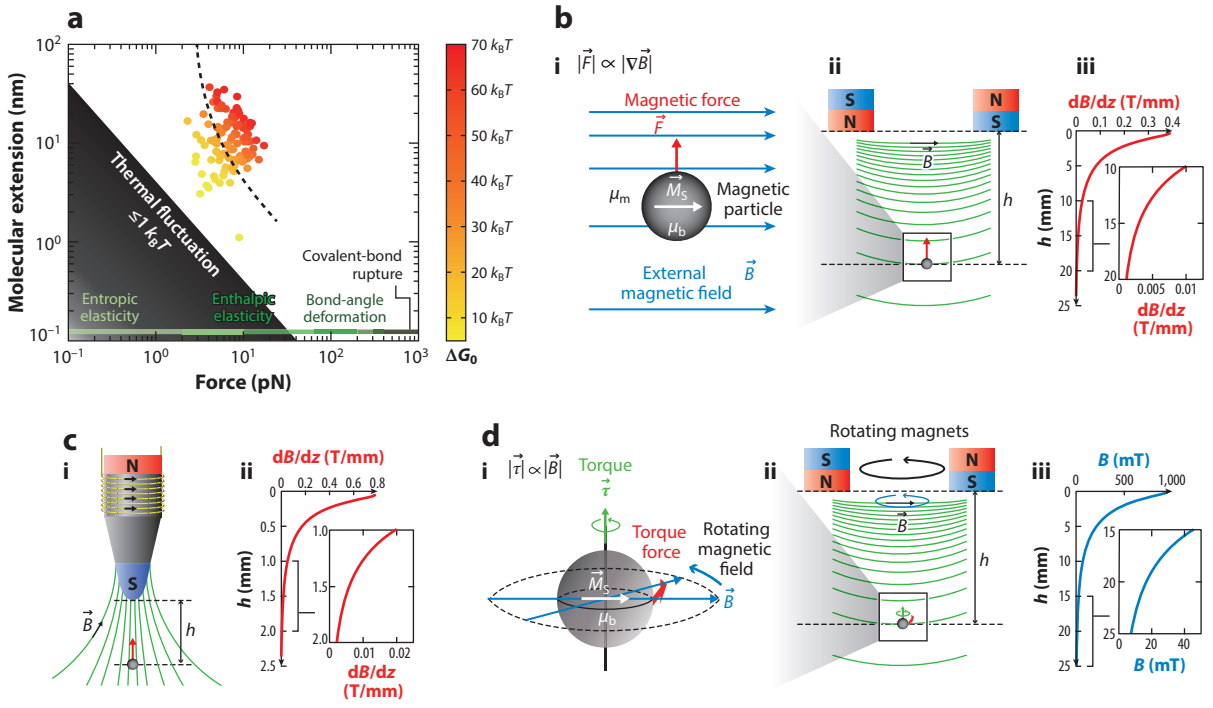

Figure 1

Force application in magnetic tweezers. (*a*) Free energy, length, and force scales for mechanical studies of protein folding. Extensions of 116 protein molecules with known folding energy values (*colored dots*; compiled from the literature) were plotted against their estimated force of unfolding. Molecular extension is calculated as the length in an unfolded linear conformation minus the size of the globular form (twice the radius of gyration). The unfolding force was estimated by dividing folding energy by the molecular extension length, assuming equilibrium and reversible processes. The black dashed line represents a data-driven curve fit using the linear dependency between folding stability (ΔG) and chain length (N) ($\Delta G = 0.08689N + 10.3985$ at 297.15K) (63, 64). (*b*) Model of the vertical force generated by an antiparallel pair of permanent magnets. Magnetic field lines and the corresponding upward field gradient are shown as a function of magnet height. (*c*) Model of the vertical force generated by one pole of an electromagnet. Magnetic field lines and the corresponding upward field gradient are shown as a function of magnet height. (*d*) Model of the torque force generated by a rotating pair of permanent magnets. Magnetic field lines and the corresponding field strength are shown as a function of magnet height.

biomolecular structures and their interactions with one another are often labile and transient, making them more dynamic and increasing their adaptability to an ever-changing environment.

To estimate the scales of forces that can modulate biological structures and their interactions, we compiled a list of the folding energies of 116 proteins and plotted these values with respect to their unfolding extensions estimated at zero force (**Figure 1*a***) (63, 64). Larger structures with longer contour lengths tend to be stabilized by higher free energies, likely due to increased numbers of interactions among the different parts of each biological polymer. Assuming a quasi-equilibrium process in the unfolding of these structures (with minimal energy dissipation), we estimated the force required by dividing the free energy values by the unfolding extensions (20, 65). Remarkably, we found the resulting force values are distributed in a narrow range between 1 and 100 pN, suggesting this as a window of force levels any force spectroscopy tool should be able to generate to control single molecules.

We then examine the conditions under which magnetic tweezers generate this range of forces. With few exceptions (66–68), most magnetic tweezer techniques take advantage of positive magnetophoresis, in which magnetic objects that induce positive magnetization vectors with relative

magnetic permeability μ_r^b ($\equiv \mu_b/\mu_0$, where μ_b and μ_0 are the permeability values of the magnetic particle and a vacuum, respectively) are embedded in buffer, cells, or tissues, all of which are essentially nonmagnetic (i.e., $\mu_m \approx \mu_0$) (69, 70). When there is a gradient in the external magnetic field, these magnetic objects tend to be attracted to the spaces where the magnetic fields are denser and characterized by higher field gradients. For a spherical magnetic particle, the magnetic force is given by

$$\vec{F} = \mu_0 V(\vec{M} \cdot \nabla)\vec{H}. \quad 1.$$

In this equation, V is the volume of the magnetic particle, $\vec{M}$ is the magnetization of the particle in unit volume, and $\vec{H}$ is the applied external magnetic field in the surrounding media. We assume a superparamagnetic particle that shows minimal residual magnetization. According to Langevin's theory of paramagnetism, when the external magnetic field exceeds a critical field strength of H_c—a condition that holds true in most magnetic tweezer applications—the magnetization vector reaches a saturated value of $\vec{M} = \vec{M}_s$, where $\vec{M}_s$ is the saturated magnetization per unit volume.

The saturated magnetization level and critical threshold for the magnetic field depend on the magnetic particle's composition and shape. The superparamagnetic particles used in these sorts of experiments typically have a radius (R_b) of 0.5–3 μm (3, 6, 71–73) and a density value (ρ_b) of 1.2–1.9 g/cm^3 (74). They also typically show a mass saturation magnetization ($|\vec{M}_{ms}| = |\vec{M}_s|/\rho_b$) of 10–100 Am^2/kg above a threshold field strength of 10–30 mT ($B_C = \mu_0 H_C$) (55, 74–76). In a saturated magnetization regime, the magnetic force exerted on the particle is linearly proportional to the magnetic field gradient ($F \propto \nabla H$). Hence, the key factors to consider are the geometry of the external magnetic field (i.e., the field gradient) and the physical parameters of the magnetic particles. This gives a rough estimate of the field gradient necessary to generate the required force (F) from the following relationship:

$$|\nabla B|_{\max} \approx \frac{3F}{\rho_b 4\pi M_{ms} R_{b,\min}^3} \quad 2.$$

Thus, to generate magnetic forces within the 1–100 pN window, the amplitude of the magnetic field gradient should be larger than ~0.01 T/mm (assuming a 2.5 pN force) (55, 76).

2.2. Different Magnet Configurations for Magnetic Pulling

A variety of magnetic tweezer setups have been devised to produce the required magnetic field gradient (3, 6, 58, 71, 73, 77–79). The most common setup employs a pair of permanent magnets arranged in an antiparallel orientation with a gap between them (**Figure 1*b***) (58, 71, 73, 78). The resulting magnetic field gradients produced by this type of setup are largely uniform in the transverse direction, especially in the gap between the magnets. Rather than trapping the particles in the center of a potential well, the magnetization vectors induced by this type of setup pull the magnetic particles monotonically and vertically toward the magnets (**Figure 1*b***) (57). Thus, in most magnetic tweezer experiments, the magnetic particles must be tethered to a nearby surface via molecular linkers.

To estimate the maximum force a magnet configuration like this can generate, we assume the use of permanent neodymium magnets with a commercially available magnetization grade of N50 (56, 80–82). When two 5-mm cubic magnets are separated by a 1-mm gap, the Biot–Savart law estimates a maximum field gradient of 0.38 T/mm as the magnetic particle asymptotically approaches the center of the gap to a distance of 0.3 mm (55). A superparamagnetic particle with a 2.8-μm diameter and the material parameters given above would then experience a force of 98 pN, ensuring that this magnetic tweezer setup can generate the force levels necessary for manipulating biological molecules. It is also important, however, that the field gradient progressively

relaxes along the vertical axis over tens of millimeters (**Figure 1*b***). Thus, measurable changes in the magnetic force occur only when the magnetic bead undergoes a millimeter-scale vertical displacement. This has vital implications in that molecular events—resulting in vertical magnetic bead displacements on a nanometer scale—do not appreciably affect magnetic force as measured with an antiparallel magnet configuration. This salient feature permits biochemical experiments at constant force levels without requiring complicated feedback instruments (see Section 3 for details).

Single magnets are used to generate more localized fields than the antiparallel magnet configuration (41, 72, 77, 83). Single magnets generate field patterns that steeply diverge in a radial manner such that the magnetic field vectors converge on the magnet's opposite pole (**Figure 1*c***). Either permanent or electric magnets can be used to generate the magnetic field, but regardless of magnet type, a tapered tip composed of permalloy or iron can be attached to the south pole to increase the local field gradient in the space surrounding the tip. Unlike the antiparallel configurations that exert uniform magnetic force along the vertical axis, single magnets exert both vertical and horizontal forces to attract magnetic particles to the center of the magnet tip.

Using an electric magnet and a tapered tip with a curvature of ∼0.02 μm, a 2.3-μm-diameter magnetic bead would experience a magnetic force of up to ∼200 pN at a distance of 10 μm, corresponding to a field gradient of ∼0.8 T/mm (72, 84). Of note, field gradients produced by single magnets decrease more rapidly than those produced by antiparallel configurations, reaching the threshold value of ∼0.01 T/mm for a bead only ∼1.5 mm away from the magnet (**Figure 1*c***). Moreover, field gradients produced by single magnets also decrease sharply as the particles are subjected to transverse displacements tens of micrometers from the center of the magnet tip. Thus, single magnet configurations can be used to deliver mechanical stimuli to highly localized regions.

Although the use of electric magnets permits the direct modulation of the magnetic field because it is proportional to the applied current, large amounts of current flowing through the electric coils can lead to problems with overheating (5). Various solutions to this problem have been suggested, including water cooling systems (5, 72, 85). It is also possible to microfabricate magnetic cores with electric wiring designed to generate multiple magnetic poles. These can produce well-defined and localized field gradients in multiple locations (86–88).

Recently, there have been technical pushes toward magnetic tweezers that work with nano-sized beads because smaller beads exhibit reduced nonspecific interactions and permit faster dynamic reporting (41, 89). To achieve the desired force window, however, these smaller nano-sized beads require more magnetization as well as stronger field gradients. Jun and colleagues used a sharper permalloy tip (with a curvature of ∼0.1 μm) to increase the field gradient surrounding the tip (41). They also changed the nano-magnetic particle core from Fe_3O_4 to $Zn_{0.4}Fe_{2.6}O_4$ (zinc-doped iron oxide magneto-plasmonic nanoparticles), which led to a tenfold higher magnetization capacity. With these two changes, Jun and colleagues were able to apply piconewton-scale forces to 40-nm magnetic particles at micrometer-scale distances. Equation 2 gives an estimated field gradient of ∼40 T/mm. This field gradient was experimentally determined to diminish within tens of micrometers, indicating a shorter reaching range by three orders of magnitude than that of the uniform field generated by an antiparallel magnet configuration. These steep force gradients mean that constant force experiments would require additional instrumentation, as is the case for optical tweezer techniques (90).

2.3. Applying Magnetic Torque

Magnetic fields can also influence magnetic objects by applying torque to induce rotational motion (**Figure 1*d***) (4, 22, 76, 84, 91, 92). Unlike the magnetic force that arises from magnetic field

gradients, magnetic torque is generated directly by the field vector represented by the following relationship:

$$\vec{\tau} = \vec{m} \times \vec{B} = \vec{r} \times \overrightarrow{F_\tau} \qquad 3.$$

Here, $\vec{m}$ is the magnetic moment (e.g., $\vec{m} = \int \vec{M} dV$, where V is the volume element), and $\vec{r}$ and $\overrightarrow{F_\tau}$ are the length of moment arm and the torque force, respectively (**Figure 1*d*, subpanel *i***).

Since ambient thermal fluctuations induce random Brownian rotation of the magnetic particles, we can estimate the level of torque required to overcome Brownian noise and rotate the particles in a robust way in a specific direction. We estimate the torque required to rotate a micron-sized particle with a radius of 1.4 μm by an angle of $\pi/2$. We further assume that an energy input 30 times as large as the ambient thermal energy (i.e., 30 $k_B T$) would be enough to accomplish the rotation despite Brownian noise. These assumptions yield an estimate of only 10 fN of torque force to produce a substantial rotation. Even considering subsaturating levels of magnetization below the critical magnetic field (H_c) (90), a magnetic field of approximately 20 mT is sufficient to induce magnetic particle rotation while overcoming thermal fluctuations. This field strength can be attained when a particle is placed as far as ~20 mm away from an antiparallel magnet configuration (76, 93) (**Figure 1*d*, subpanel *iii***).

These rough estimates suggest magnetic tweezers can induce the rotation of magnetic particles at far larger distances than those at which piconewton-scale pulling forces can be applied. This access at a greater distance stems from the fact that the torque is being generated directly by the magnetic field. As was also found during the development of nuclear magnetic resonance techniques, it is much easier to increase the magnetic field strength than steepen the magnetic field gradient. It has been demonstrated that by increasing the field strength, the rotational motion of magnetic nanoparticles could be induced as far as 70 cm away from the magnets (92).

3. DEVELOPING HIGH-RESOLUTION SINGLE-MOLECULE MAGNETIC TWEEZERS

3.1. Physical Principles

With their capacity to apply force and torque at levels suited to the modulation of the structure and function of biological molecules, magnetic tweezers have evolved to be a prominent technique for single-molecule force spectroscopy (7). To monitor mechanical responses, magnetic tweezers rely on video-based tracking of bead positions (54). Bright-field images are analyzed continuously to extract the three-dimensional coordinates of tracked beads (**Figure 2*a***). Accurate tracking along the vertical axis (mirroring force-induced changes in molecular extension) requires clear diffraction patterns of beads placed slightly out of focus by design (6, 54). As a bead moves away from the imaging plane in either direction, the concentric ridges in its diffraction image undergo radial expansion. By moving the objective lens in regular steps with a nano-positioning device (i.e., using a piezo-driven objective lens), a precalibrated collection of diffraction images can be generated. Real-time images of the same bead are then compared to its calibrated intensity profile. Although the calibration patterns are sparsely spaced 50–100 nm apart along the vertical axis, the associated changes in the radial profile are significant enough and distributed over enough pixels in high-magnification images that even minute differences induced by subnanometer displacements can be reliably detected (6).

The use of magnetic tweezers for interrogating single biological molecules was first demonstrated by Bustamante and colleagues (3). In this landmark paper, a single double-stranded DNA molecule, tethered to a surface, was stretched and relaxed. Since this pioneering study, most

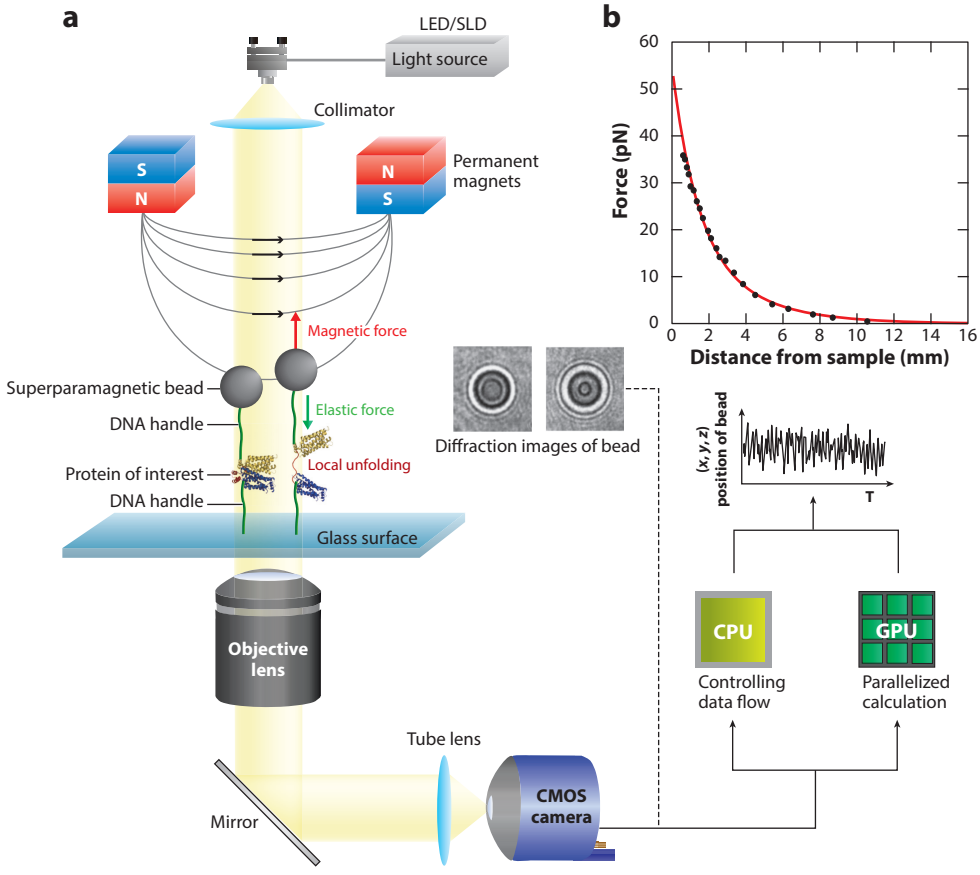

Figure 2

High-speed magnetic tweezer concept. (*a*) Schematic of the setup. Single protein molecules of interest are suspended between a glass surface and magnetic beads. They are manipulated through the controlled motions of a pair of permanent magnets. The beads are illuminated by a collimated beam of light from an LED or SLD that is carefully aligned to pass through the 1-mm gap between the magnets. The resulting diffraction patterns from the beads are imaged with a high-speed CMOS camera at 100–1,200 Hz. The frames acquired are processed collaboratively in real time by the CPU and GPU to extract the three-dimensional coordinates of each bead (57–59). (*b*) The magnetic forces generated in this setup. Force was measured in this setup as a function of magnet height and fitted to a double-exponential model (*red*) (81). Abbreviations: CMOS, complementary metal-oxide semiconductor; CPU, central processing unit; GPU, graphics processing unit; LED, light-emitting diode; SLD, superluminescent diode.

studies using the magnetic tweezer technique have focused on the elastic properties of nucleic acids, as well as the biochemical functions of enzymes interacting with nucleic acids (10, 94, 95). Because these studies typically used nucleic acids such as λ-phage DNA with tens of kilobase pairs, relevant changes in their extension values occur on a scale of hundreds of nanometers or even more. One of the unique abilities of the magnetic tweezer technique is the application of torque. This can be used to accumulate torsional stress in double-stranded DNA molecules to induce the formation of supercoils (4, 96, 97). Supercoiling is also accompanied by large extension changes spanning hundreds of nanometers in the case of kilobase-long DNA molecules. In addition, as discussed in the preceding paragraph, the measurement bandwidth of the magnetic tweezer

technique has long been limited by its requirement for image-based magnetic bead tracking, which makes its measurements intrinsically slower than those of optical tweezers or AFM (17). Most earlier applications of the magnetic tweezer technique were limited to measuring large changes occurring under quasi-equilibrium conditions in which force levels varied slowly over seconds to minutes (3, 10, 19).

Yet, when combined with higher measurement resolution and bandwidth, magnetic tweezers have distinct technical advantages that are not easily paralleled by other single-molecule force spectroscopy tools. In the uniform field generated by an antiparallel magnet configuration, the magnetic field gradient slowly relaxes on a millimeter scale (55). With optical tweezers and AFM, the force levels change steeply over the typically submicrometer scales of the focused gaussian beams and AFM cantilever tips (17). In contrast, for magnetic tweezers, the force level is precisely controlled on the same length scale over which the magnetic field gradient varies, and this millimeter-scale control of the magnet's position is readily accomplished with simple motorized controls (**Figure 2*b***) (81). At the same time, because molecular events occurring in the target molecules involving extension changes on a nanometer scale do not significantly alter the force levels experienced by the magnetic beads, magnetic tweezer experiments can be done under essentially constant force levels (55). Because the energy landscapes governing biological structures and processes shift gradually as the forces applied increase (98–100), experiments in which applied force levels vary continuously have to contend with inevitable changes in the shape of the energy landscape being studied. In contrast, magnetic tweezers provide a platform to directly probe the energy landscapes that govern biological phenomena at fixed levels of mechanical tension.

This important advantage justifies the work being done to push the magnetic tweezer technique toward higher-bandwidth measurements reaching a few kilohertz of sampling frequency accompanied by nanometer precision in magnetic bead tracking. In fact, significant efforts have been made in the past decade to improve the spatiotemporal resolution of magnetic tweezers and unleash their full potential (57–59). Several pioneering research groups have unambiguously demonstrated tracking of millisecond-scale biological events with nanometer precision, enough to decipher delicate conformational changes in tiny globular proteins (79, 101). Not only that, but these measurements allowed for the direct reconstruction of the associated free energy landscapes (73, 102). We briefly summarize the theoretical considerations of measurement resolution in the magnetic tweezer technique and then outline recent developments toward building magnetic tweezers with higher resolution and tracking speed.

The fundamental limits of temporal and spatial resolution in magnetic tweezer experiments are shared by all single-molecule force spectroscopy techniques and discussed in previous excellent reviews (17, 103). We therefore provide a summary of key results using the magnetic tweezer technique. In magnetic tweezer experiments, single target molecules are tethered to magnetic beads, usually via double-stranded DNA handles (7). The structural changes in the target molecules are then transmitted through these DNA handles and reflected in the vertical displacements of the tethered bead. Thus, the dynamics of any molecular transitions are low-pass filtered by the response time of the bead-handle construct, and the bead height measurements are limited by the Brownian motion experienced by the beads and handles. In practice, the fundamental limits of temporal and spatial resolution are further compromised by the technical limitations of the measurement apparatus, namely the finite speed of camera-based tracking and the bead tracking noise.

Let us consider a magnetic bead of mass m. Its motion in a fluid experiences a viscous drag governed by the drag coefficient γ. The momentum relaxation time for the translational Brownian motion of the bead (i.e., the exponential decay in momentum caused by collisions with fluid molecules after the bead initially gains momentum) is given by m/γ. This value falls at approximately 1 μs or below for typical magnetic microparticles. On significantly longer

timescales, the bead's motion in a low-Reynolds-number regime can be described by the overdamped Langevin equation:

$$0 = -\gamma \dot{z}(t) - k_z z(t) + \xi(t). \quad 4.$$

In this equation, $z(t)$ is the vertical position of the bead and $\xi(t)$ is the thermal force from random Brownian collisions with solvent molecules. Although $\xi(t)$ varies over time, such variation also occurs on a much faster timescale (10^{12}–10^{14} Hz) than the bandwidth of our measurements. The second term accounts for the linear restoring force arising from the tether with a spring constant k_z. It shows that, for small displacements around the equilibrium position, the elasticity of the tether is an approximation of its harmonic potential. This differentiates magnetic tweezers from other single-molecule force spectroscopy techniques, in which the restoring force arises directly from trap stiffness rather than from tether elasticity.

One can imagine that once a nanoscale molecular event (e.g., DNA hairpin unzipping, chemical bond breakage, or protein unfolding) occurs at $t = 0$, the bead height $z(0)$ moves away from its equilibrium position. Assuming that the structural transitions of molecules are instantaneous [they do take a small but finite amount of time (31)], the bead relaxes to a new equilibrium position, the trajectory of which is given by the solution of Equation 5:

$$z(t) = z(0)\exp(-t/\tau_c) + \frac{1}{\gamma}\int_0^t \mathrm{d}t' \exp[-(t-t')/\tau_c]\xi(t'). \quad 5.$$

In this equation, the first term describes the exponential decay with a time constant $\tau_c = \gamma/k_z$, and the second term indicates the accumulated effects of random forces along the trajectory, exhibiting the same decay time constant. The drag coefficient can be estimated from the Stokes–Einstein equation $\gamma = 6\pi\eta r$ for a spherical particle of radius r in a solution of viscosity η. Thus, smaller beads with smaller γ values are preferred because they permit faster monitoring of molecular events.

From Equation 5, we find that the elasticity of a tether, represented by k_z, critically determines the dynamic response of the bead–tether construct. Since most magnetic tweezers use double-stranded DNA fragments as molecular tethers, the worm-like chain model relates the extension of a tether l to an applied force F (104). This model is represented as follows:

$$\frac{Fl_\mathrm{p}}{k_\mathrm{B}T} = \frac{1}{4(1-l/l_0)^2} - \frac{1}{4} + \frac{l}{l_0}. \quad 6.$$

In this equation, l_0 and l_p are the contour and persistence lengths of the tether, respectively. The force-dependent stiffness would then be represented as follows:

$$k_z = \frac{\partial F(l)}{\partial l} = \frac{k_\mathrm{B}T}{2l_\mathrm{p}l_0}\left[2 + \left(1 - \frac{l}{l_0}\right)^{-3}\right]. \quad 7.$$

Thus, the stretching elasticity of DNA is not linear over the extension regime but is a function of its full length l_0 and its extension l at the time of a given measurement. Using a shorter tether (i.e., smaller l_0) or stretching the tether to its full extent (l/l_0 approaching 1) increases k_z and provides faster relaxation. The application of higher forces to trigger further tether stretching is not always a viable option, depending on the biological system of interest. This means using shorter DNA tethers is generally a better strategy. We plot the calculated values for the relaxation time constant τ_c in **Figure 3*a*,*b*** using representative parameters. These plots indicate that the use of submicrometer tethers guarantees submillisecond response times even in a low-force regime of 1–5 pN. It is notable from Equation 6 that the tether is already extended to over 80% of its contour length at 1 pN of force because the elastic entropy of the tether polymer is effectively

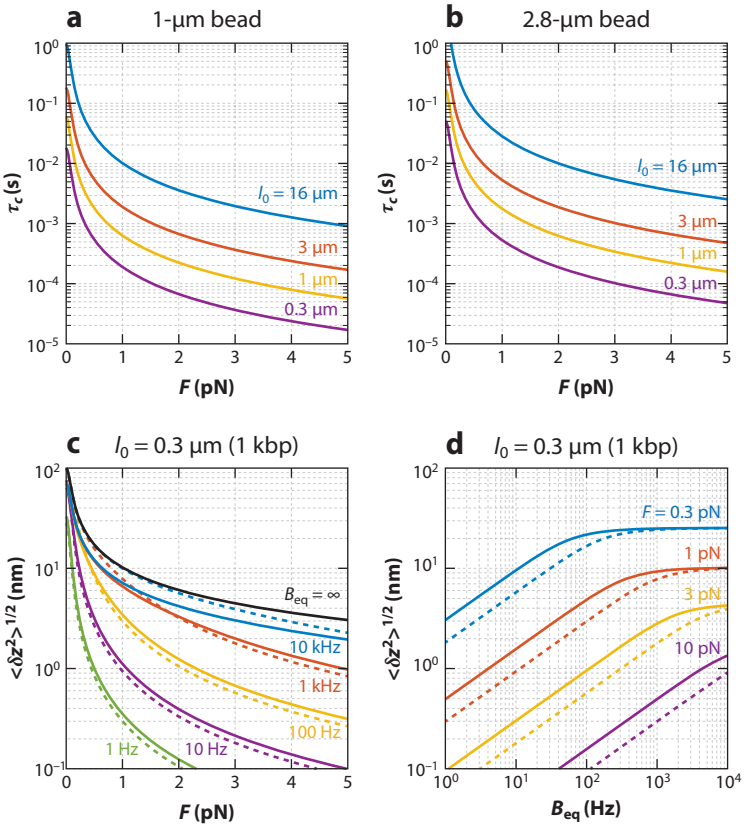

Figure 3

Thermal fluctuations in bead position limit the spatiotemporal resolution of magnetic tweezers. (*a*,*b*) Characteristic thermal fluctuation timescale (τ_c). τ_c represents the exponential decay constant for the bead height fluctuations calculated for the designated bead radii and tether lengths (l_0) as functions of applied force. (*c*,*d*) The magnitude of the thermal fluctuations calculated for various conditions of applied force (F) and measurement bandwidth (B_{eq}). $\sqrt{\langle \delta z^2 \rangle}$ values were estimated from Equation 9 for the 2.8- (*solid*) and 1-μm (*dotted*) beads attached to 0.3-μm tethers. For all panels, the tethers were assumed to be double-stranded DNA fragments that follow a worm-like chain model of $l_p = 45$ nm (104).

suppressed at force levels above 1 pN. In the same force range, the response time is also steeply reduced as the tether is straightened (**Figure 3*a*,*b***).

We used the Stokes–Einstein equation for our calculations, but the use of submicrometer tethers increases the viscous drag on magnetic beads near the surface. This necessitates the use of Faxén's law to correct for the viscous drag component (105). For the same reason, the vertical drag is not equal to the drag arising from lateral movements in proximity to the surface. These corrections generally increase the effects of viscous drag, resulting in reduced response times, especially for short tethers with small extensions.

Given that the bead–tether response is fast enough to reflect dynamics of biophysical interest, the next question is whether magnetic bead tracking is precise enough to detect molecular events of interest above the level of the Brownian noise that arises in the motion of the bead–tether construct. Because thermal forces can be treated as white noise with a constant, single-sided power

spectral density (PSD) of $4\gamma k_B T$ (7), the fluctuations of the bead–tether construct, governed by Equation 4, follow the Lorentzian function:

$$S_z(f) = \frac{k_B T}{\pi^2 \gamma (f_c^2 + f^2)}. \quad 8.$$

In this function, the cutoff frequency $f_c = 1/(2\pi\tau_c) = k_z/(2\pi\gamma)$ that governs the mechanical response of the bead–tether construct exactly matches the inverse of the dynamic response time derived in Equation 5. Thus, any thermal fluctuations occurring faster than the dynamic response time are filtered out because the bead–tether construct cannot respond to these fast-evolving fluctuation components. The PSD in Equation 8 contains the frequency content of the system across the entire bandwidth. One can integrate it over a relevant frequency range to estimate the magnitude of any fluctuations as follows:

$$\sqrt{\langle \delta z^2 \rangle} = \left[\int_0^{B_{eq}} S_z(f) df \right]^{\frac{1}{2}} = \left[\frac{2k_B T}{\pi k_z} \tan^{-1} \left(\frac{B_{eq}}{f_c} \right) \right]^{\frac{1}{2}}. \quad 9.$$

Here, $\sqrt{\langle \delta z^2 \rangle}$ represents the time-averaged thermal fluctuations in the z direction. In using this equation, the infinite-bandwidth observation (i.e., $B_{eq} = \infty$) is a special case that corresponds to a measurement without any time averaging. In this infinite-bandwidth measurement, the fluctuation magnitude is reduced to $\sqrt{\langle \delta z^2 \rangle} = \sqrt{k_B T / k_z}$, which is consistent with the prediction from the equipartition theorem. Plugging $\langle \delta z^2 \rangle = k_B T / k_z$ into Equation 7 produces the following:

$$\langle \delta z^2 \rangle = \frac{2 l_p l_0}{2 + (1 - l/l_0)^{-3}}. \quad 10.$$

This equation has the crucial implication that using a short DNA tether (and/or stretching the tether more fully) not only reduces the dynamic response time but also reduces the thermal noise associated with determining the vertical position of the magnetic bead.

For actual measurement systems, the finite acquisition rates of cameras set B_{eq} to a finite value, leading to an averaging over a time window of $1/B_{eq}$ (in seconds). This leaves out high-frequency fluctuations and thus reduces the $\sqrt{\langle \delta z^2 \rangle}$ value, offering improved resolution for bead tracking. **Figure 3*c*,*d*** plots the expected thermal fluctuations for 1-kbp tethered beads under the indicated conditions of applied force and measurement bandwidth. Remarkably, these plots indicate that nanometer precision ($\sqrt{\langle \delta z^2 \rangle} \sim 1$ nm) is feasible with reasonable parameters often used in single-molecule magnetic tweezer experiments. For example, to resolve nanoscale changes in protein structures, magnetic beads with a 2.8 μm diameter can be tethered to a 1-kbp piece of DNA and monitored under 5 pN of tension at a sampling frequency of 100 Hz.

We note that these fundamental limits on measurement resolution may not be reached in practice because of deleterious effects independent of the sample, effects like mechanical and thermal instability of the setup or corruption of bead images due to light scattering in the background. For instance, highly concentrated and heterogeneous mixtures of proteins and lipids tend to cause significant low-frequency fluctuations in background intensity, severely diminishing overall measurement resolution. Artifacts arising from the finite acquisition frequencies of the specific camera being used should also be considered and corrected (82, 106, 107).

Additional complications arise from the rotational tumbling of magnetic beads. The orientations of individual magnetic beads are pinned along the direction of the magnetic field due to energetic preference (76). When the bead's center of mass is driven away from the molecular axis of its tether, rotational fluctuations associated with this movement are again governed by another Langevin equation coupled to translational movement in the vertical direction (108). This effect introduces additional variability in measurement noise.

3.2. Construction of High-Resolution Single-Molecule Magnetic Tweezers

The discussion in Section 3.1 suggests that using a short, submicrometer tether at moderate force levels (~5 pN) allows the bead–tether to respond fast enough to report molecular dynamics at a submillisecond scale. Time averaging of the bead position at 1 kHz reduces the random noise from thermal fluctuations of the bead–tether construct down to ~1 nm, providing enough measurement precision to track changes on a molecular scale (**Figure 3**). Thus, despite all of the technical challenges involved in improving the spatiotemporal resolution of camera-based bead tracking, high-speed magnetic tweezers permit observations of subtle molecular changes in single target molecules.

The key technical requirements for high-resolution bead tracking in the magnetic tweezer technique are (*a*) a fast camera for bead imaging, (*b*) a bright light source for illumination, and (*c*) a seamless workflow for image acquisition and real-time processing that includes an efficient algorithm for three-dimensional tracking of the bead position. The first requirement, arguably the most critical among those mentioned, has largely been resolved with recent advances in complementary metal-oxide semiconductor (CMOS) image sensors. The advantages of high-speed CMOS cameras for single bead tracking as an alternative to photodiode position sensors were explored earlier for use with the optical tweezer technique (109–111). CMOS cameras are favored over cameras based on charge-coupled devices, mainly because of their acquisition speed (112). Narrowing the field of view to specific regions of interest (e.g., those containing magnetic beads) further increases this already faster acquisition rate because of the parallel nature of CMOS pixel readout designs (59).

The light source for bead illumination also plays a crucial role, particularly in high-speed imaging. In standard setups running at ~100-Hz frame rates, a bright light-emitting diode (LED) provides enough photons, when tightly focused on the imaging plane, to generate clear bead images with minimal tracking noise. When the acquisition rate rises above 1 kHz, however, the number of photons reaching the sample becomes a limiting factor. Thus, an optimal light source should generate strong diffraction patterns while providing adequate power, a short coherence length (to minimize interference speckles), and a single spatial mode. Several options have been explored, including a high-power fiber-coupled LED (58), a mercury lamp (59, 111), a superluminescent diode (58, 113), and a modulated laser diode (58, 114).

At the same time, the framework for efficient tracking has been empowered with the advent of parallel computing with graphics processing units (GPUs) (57–59, 115). In three-dimensional bead tracking, there is a trade-off between tracking accuracy and image processing speed. The more pixels a single bead image contains, the easier it is to localize the bead in a two-dimensional plane, but all those pixels also slow down the overall image analysis. Another trade-off arises in tracking multiple beads in a larger field of view for high-throughput measurements (75, 78, 101, 115, 116). In general, outsourcing image processing to the GPU releases the central processing unit from some of its computational burden, facilitating the integration of a magnetic tweezer setup with additional components and permitting more complex experiments.

Since many factors influence the spatial resolution of bead position measurements in the magnetic tweezer technique, it is difficult to directly compare the various platforms developed by different research groups. In particular, the thermal motion of the bead–tether constructs varies considerably depending on measurement configurations such as bead size, tether length, and applied force. Moreover, as with other position measurements, spatial and temporal resolutions in the magnetic tweezer technique are coupled to one another because using a wider time window for averaging bead positions improves the spatial resolution, but this comes at the expense of

measurement bandwidth. For these reasons, researchers standardize their reports of resolution using power spectrums and Allan variance measurements (80, 117, 118).

We conclude this section by introducing some recent achievements in the development of high-resolution magnetic tweezers that have maintained all of the unique strengths of the technique. These include efforts aimed at improving the rate at which the force exerted by the single-molecule tweezers can be changed, a parameter conventionally limited by the translation motors that drive the motion of the permanent magnets (79, 119). In our discussion of high-resolution magnetic tweezers, however, we limit our scope to improving the speed and accuracy of bead tracking.

In Lansdorp et al. (57), Saleh and coworkers reported results from a system that combined a high-speed camera with a superluminescent diode. This enabled them to record bead images at rates of up to ~35,000 frames per second. They also improved the speed of their bead tracking algorithm by using GPUs for parallel image analysis. This setup was tested with a plain 1.6-kbp dsDNA and a DNA hairpin construct, and it proved capable of dissecting the dynamics of hairpin transition on a millisecond time scale.

Seidel and coworkers reported camera-based tracking of magnetic beads illuminated with a fiber-coupled mercury arc lamp (59). Their work showed that GPU-assisted image analysis makes it possible to perform real-time and long-term tracking of multiple beads while still imaging enough pixels for subnanometer tracking accuracy.

Another instrument with similar spatiotemporal resolution was developed by Dekker and coworkers (58, 115). Dulin et al. (58) built a magnetic tweezer apparatus that can track single beads at rates of up to 8 kHz and characterized its ability to track DNA hairpin dynamics. Their work used a megahertz-modulated laser for uniform, high-intensity illumination, essentially eliminating all concerns about the light source. Also, by incorporating GPU-based image analysis, they were able to accurately track hairpin transitions and sort out subtle interference from free-floating nucleotides in solution. A benchmark high-resolution data set generated with this setup was recently made publicly available (107). Overall, the state-of-the-art in the magnetic tweezer field offers sub-Ångstrom tracking precision for surface-fixed beads and can resolve the thermal limits of subnanometer changes in tethered beads over a bandwidth of 1–10 Hz.

Yoon and coworkers focused on improving high-resolution measurements in a lower-force regime (1–10 pN) with the use of short DNA tethers (typically two dsDNA handles of ~500 bp or ~170 nm), thereby achieving nanometer resolutions with a millisecond-scale sampling time. In particular, Yoon and colleagues systematically addressed the technical hurdles associated with using short tethers with the magnetic tweezer technique (113). A theoretical framework describing the behavior of finite tethers in single-molecule tweezer experiments was introduced by Seol et al. (120). This framework proved crucial in interpreting the observed dynamics of bead–tether constructs. For example, Seol et al. were largely able to account for the low-force deviations in the force-extension behavior they observed by considering the geometric constraints of the bead–tether constructs. At the same time, the rotational displacements arising from magnetic anisotropy of individual magnetic beads introduce both static offsets and dynamic fluctuations in bead-height measurements (108). These undesirable effects are more pronounced in a low-piconewton regime, complicating the measured force-extension profiles of short DNA constructs. By carefully correcting the errors associated with extension and force measurements, a thorough procedure for using submicrometer tethers down to 198 bp has been established. This approach has been used successfully for investigating DNA mechanics (113), protein complex conformations (121), enzymatic processes (122), and membrane protein folding (73).

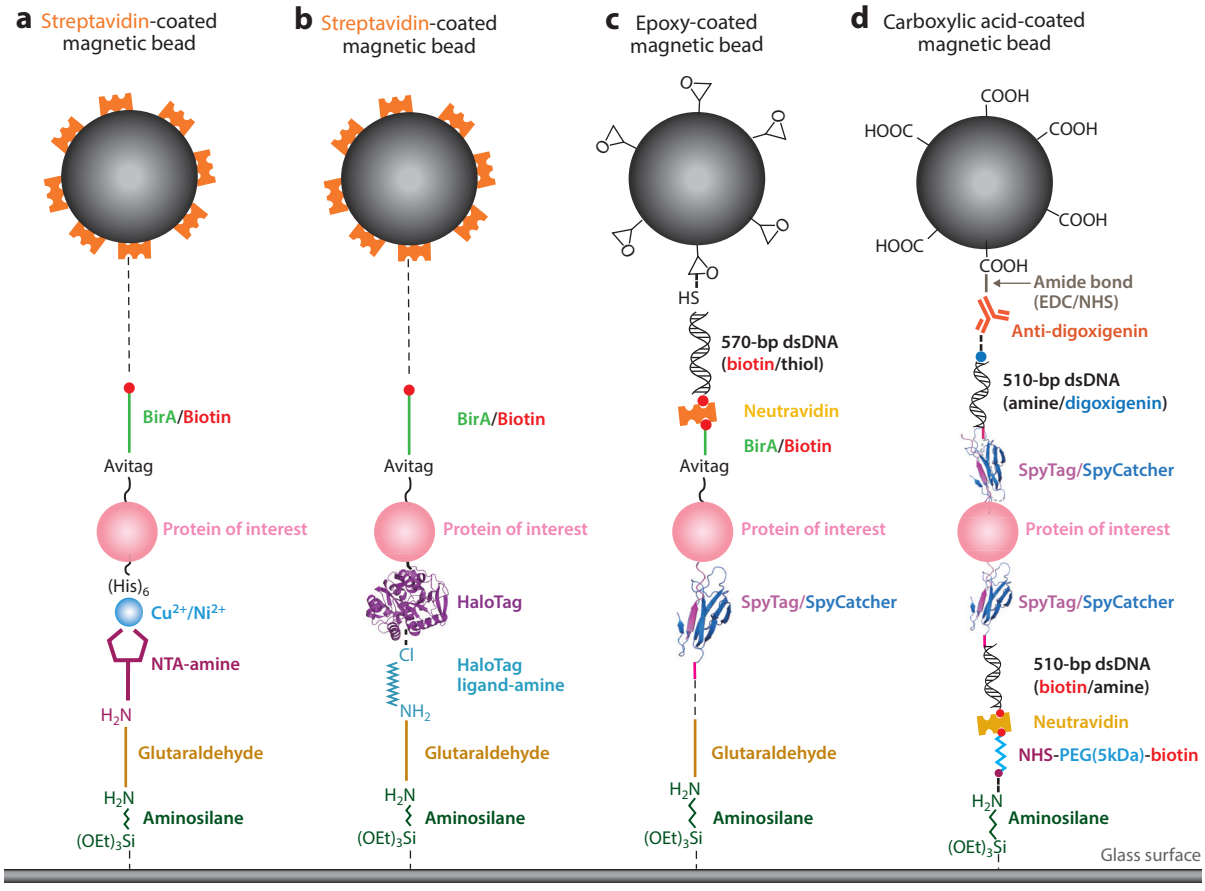

Figure 4

The designs for bead–tether constructs used in magnetic tweezer experiments with proteins. Four representative structures found in the literature are shown with the chemical moieties involved in their tethering. (*a*) Avidin-based bead attachment and metal-NTA-based surface attachment (38, 39, 71). (*b*) Avidin-based bead attachment and HaloTag-based surface attachment (79, 102, 129–131). (*c*) Epoxy-based bead attachment and SpyTag-based surface attachment. The avidin-biotin system was additionally used to include an upper DNA handle (132–134). (*d*) Anti-digoxigenin-based bead attachment and avidin-based surface attachment. The SpyTag/SpyCatcher system was additionally used to include two DNA handles (73). Abbreviations: EDC, *N*-ethyl-*N*′-(3-(dimethylamino)propyl)carbodiimide; NHS, *N*-hydroxysuccinimide; PEG, polyethylene glycol; NTA, nitrilotriacetic acid.

4. APPLICATIONS OF MAGNETIC TWEEZERS TO BIOLOGY

4.1. Designing Pulling Constructs

The application of high-resolution magnetic tweezers to biological questions requires stable constructs for pulling single biomolecules (123). Because magnetic tweezers apply pulling force rather than creating a harmonic well (57), two separate sites on a single target molecule must be conjugated to a magnetic bead and to a surface, respectively (7). Only the part of the target molecule between these two linkage sites, which become aligned parallel to the force-application axis when placed under tension, can be subjected to tension (**Figure 4**). Thus, the linkage sites control the points of force application and their careful selection provides the opportunity to dissect the mechanical responses of different parts of the target molecule (37, 124). Although some of the earlier

attempts at single-molecule force spectroscopy relied on nonspecific adsorption to attach single molecules to probes or handles (14, 125), most of the recent tweezing experiments are based on site-specific conjugation of handles to selected amino acid residues. In this section, we examine the various approaches that can be used to assemble a construct for pulling single molecules in magnetic tweezer experiments.

Diverse functional groups can be readily delivered to the ends of double-stranded DNAs using chemically modified DNA primers during amplification via PCR (113, 123). These functional groups can then be used to conjugate the DNAs to other parts of the construct. In contrast, incorporating similar conjugation points into a protein in a site-specific manner is much more difficult. Because proteins typically have multiple native cysteine residues, simple cysteine–maleimide chemistry cannot deliver handles to single sites in a target protein. Several single-molecule tweezer studies have used the incorporation of unnatural amino acids to provide conjugation sites, but this requires specialized expression systems (37, 126). Typically, most studies use protein tag fusion to introduce a linkage site at a predefined location, usually the N or C terminus of the target protein.

In early magnetic tweezer studies, researchers used 6×His (His-Tag) for surface immobilization (**Figure 4*a***) (38, 39, 71). First, chelator molecules (e.g., nitrilotriacetic acid) were covalently attached to silanized glass surfaces via glutaraldehyde crosslinking, and then divalent metal ions (Cu^{2+}/Ni^{2+}) were added (**Figure 4*a***). To attach the other end of the target protein to a magnetic bead, AviTag was covalently biotinylated by the *Escherichia coli* biotin ligase BirA during protein expression (38, 39) or after purification (71). Finally, streptavidin-coated magnetic beads were attached to the target protein via the strong biotin–streptavidin bond.

Although the mechanical properties of several force-sensing proteins have been explored using His-Tag-based constructs (38, 39, 71), the use of His-Tags in the formation of stable pulling constructs has two major disadvantages. First, although the imaging surface is passivated after metal ion coating, His-Tags are still prone to nonspecific interactions. Second, His-Tag-mediated conjugation is noncovalent and thus provides limited bond strength. To overcome these limitations, several attachment strategies that provide for stronger and more specific protein construct immobilization have been developed. One of these strategies uses HaloTag, a 33-kDa engineered dehalogenase enzyme (**Figure 4*b***) that forms a specific covalent bond with a chloroalkane-based ligand (127). One advantage of the HaloTag system is that the covalent reaction occurs directly between the ligand and HaloTag without requiring any additional reagents or enzymes. Moreover, the strength of the resulting bond allows prolonged observation of the target protein for several days or even weeks (128).

Despite the many advantages of the HaloTag conjugation system (79, 102, 129–131), HaloTag occasionally unfolds at high force, resulting in an extension change of tens of nanometers (102). This undesirable unfolding of the tag itself could easily be misinterpreted as a positive signal when the relevant extension changes are of a similar length, complicating the analysis of the magnetic tweezer experiment. One alternative strategy for overcoming this issue is the use of the SpyTag/SpyCatcher split-protein system (**Figure 4*c***) (132–134). This system relies on the formation of an isopeptide bond between a short peptide (SpyTag) and a larger protein (SpyCatcher) (135). Like the HaloTag system, the formation of the covalent SpyTag–SpyCatcher bond does not require any additional reagents. Since bond formation between SpyTag and SpyCatcher is fast, target proteins carrying SpyTags are introduced to a surface coated with SpyCatcher to directly induce bond formation. One group used a construct with SpyTag and AviTag at opposite ends to study the unfolding behavior of single ZPSG domains of ZO-1 proteins at force levels up to ∼100 pN (132).

To study proteins that are prone to nonspecific interactions with the imaging surface (e.g., membrane proteins), surface-passivation protocols developed for use in the field of

single-molecule fluorescence spectroscopy can be employed (**Figure 4*d***) (73). Specifically, amino-silanized glass slides are coated with a mixture of methoxy-polyethylene glycol (PEG)–hydroxysuccinimide (NHS) and biotin–PEG–NHS, with an excess of methoxy-PEG molecules for passivating the surface and far fewer biotin–PEG molecules to serve as binding sites for later conjugation. To minimize the direct contact of the target proteins with either the magnetic beads or the surface, two 510-bp double-stranded DNAs are attached to the N and C termini of the target proteins using the SpyTag/SpyCatcher system. Since SpyCatcher is a small protein molecule without any native cysteines, an artificial cysteine residue can be introduced between the purification tag and the SpyCatcher to induce DNA linkage via the cysteine-maleimide reaction (73, 136). The linked DNA handles then also serve as an indicator for proper assembly of the pulling construct because poorly assembled ones fail to show the typical force-extension curves of ∼1-kbp DNAs nor do they show substantial Brownian motion in the absence of tension. The other ends of these DNA handles are modified with biotin or digoxigenin, which are used to attach the DNA handles to the magnetic bead and for surface immobilization, respectively.

4.2. Applying Magnetic Tweezers to Force-Dependent Biological Processes

As more groups apply the high-resolution magnetic tweezer technique, it has repeatedly proven effective at solving otherwise intractable biological problems (38, 73, 101, 102, 129, 131). Because there are excellent reviews about the use of magnetic tweezers for studying nucleic acids and their conformational changes evoked by enzymes (7, 137), we focus here on recent uses of single-molecule magnetic tweezers to directly investigate the conformational changes that occur in individual proteins.

Many of these pioneering studies have explored cutting-edge questions in biology regarding how cells generate, sense, and modulate tension (38, 102, 129). The binding of chemical ligands has long been the prevailing paradigm for the delivery of biological signals. However, because chemical ligands suffer from continuous dilution owing to Brownian motion, mechanical force is emerging as a novel class of biological signal. The biological systems that use these signals can exchange mechanical cues between their different components in a much more localized manner without any spatial dilution (60, 61, 138).

Titin, which is a major protein component of muscle sarcomeres, is a good example showing such a force-responding phenomenon (139). Titin's immunoglobulin (Ig) domain was the first protein target studied by single-molecule force spectroscopy, and its mechanical properties have since been thoroughly investigated with many different techniques (14, 139–141). Under a high pulling rate of 1 μm/s (a force loading rate of ∼1,000 pN/s) (14), titin Ig domain unfolding has typically been observed above the 100-pN level, far from equilibrium conditions. In contrast, Yan and colleagues performed force-clamp measurements using single-molecule magnetic tweezers at a uniform force level of 4.5 pN and observed both unfolding and refolding events of Titin's Ig domain (102). This drastic reduction in the relevant force level indicated that the folding reactions occurred under quasi-equilibrium conditions with minimal free energy dissipation, permitting direct reconstruction of the governing energy landscape. With a millisecond time resolution, Fernandez and colleagues determined how fast refolding occurred and estimated the power generated by the folding of a single Titin Ig domain, which reached 6,000 zW (129). This remarkable number suggests Titin proteins may actively function in muscle contraction as much more than mere passive springs.

Another example of a cellular force-generating machinery is the focal adhesion, a large protein assembly that attaches cells to the surrounding extracellular matrix. Although many protein components of focal adhesions have been identified, it remains unclear how mechanical cues from the

outside are transduced to affect downstream cell-signaling circuits, i.e., how the mechanical signal is converted to a chemical one (142). In a landmark paper by Sheetz, Fernandez, and coworkers, a magnetic tweezers setup was used to pull single molecules of talin, the protein that connects integrin receptors to the actin cytoskeleton (38). Under 12 pN of tension, the talin rod domain unfolded, exposing a previously hidden vinculin-binding site. This group further observed that excessive tension inhibited vinculin binding by removing the secondary structure of the binding site, indicating the existence of an optimal force window for facilitating talin–vinculin binding (131). The single-molecule tweezer technique has been used to explore the force-dependent behaviors of many proteins, such as α-catenin (39), ZO-1 (132), formin (143), and dystrophin (144), clarifying the molecular mechanisms underlying their related mechanobiological processes.

Protein folding remains a major field of inquiry in modern molecular biology. In conventional bulk biochemical assays for protein folding, high temperature or chemical denaturants are first added to induce an unfolded state in the target proteins. The heat or chemical denaturants are then removed to induce protein refolding (145). Since bulk assays like these typically rely on optical signals, such as absorption at a certain wavelength or native tryptophan fluorescence, they cannot provide detailed conformational information. Mutations are introduced into the target proteins, and the corresponding changes in the bulk biochemical readouts are translated into rough structural information, a process that requires some rather large assumptions (146). In contrast, single-molecule force spectroscopy applies mechanical tension to induce target protein unfolding. Then, under piconewton-scale tension, the unfolded part takes on an extended conformation (147, 148). Thus, unlike with bulk biochemical readouts, the unfolding/folding readouts from single-molecule force spectroscopy techniques can directly reflect the number of residues in the unfolded part of the protein (73). In particular, the force-clamp capability of the magnetic tweezer technique permits the observation of both folding and unfolding events at a set force level, which permits the direct estimation of the protein's equilibrium properties, including its folding energy landscape. The folding properties of a variety of proteins, such as BapA (149), protein L (79, 150), filamin A, and von Willebrand factor (101) have now been studied with single-molecule magnetic tweezers.

Of note, the single-molecule magnetic tweezer technique has recently been applied to the folding of multi-pass helical membrane proteins, which are notoriously difficult to study (73). With remarkable advances in cryo–electron microscopy (cryo-EM), the tertiary and quaternary structures of multi-pass membrane proteins are now being revealed at an unprecedented pace (151). In these complex structures, transmembrane helices (TMHs) pack close to one another, permitting elaborate conformational changes that regulate the flow of information and materials across the cell membrane (152, 153). Regardless of their importance, however, very little is still known about how these multi-pass membrane proteins form in the endoplasmic reticulum membrane (154).

Yoon and coworkers serially applied three different force-application protocols based on single-molecule magnetic tweezers to elucidate the folding pathways of multi-pass membrane proteins (73). The N and C termini of multi-pass membrane proteins were fused to SpyTags and attached to magnetic beads and the imaging surface via two double-stranded DNAs (510 bp each) (**Figure 5*a***). In the first protocol, over 20 pN of mechanical tension was applied to induce full mechanical unraveling of the single membrane protein molecules, resulting in unstructured polypeptides (referred to as the U_c state) (**Figure 5*b***). The applied force was subsequently lowered to approximately 5 pN to initiate membrane protein refolding. Rather than a monotonic downward march toward the native state (*N*), the resulting refolding process showed many upward and downward steps. Hidden Markov modeling was then used to identify the obligate intermediates (**Figure 5*c*,*d***). While this first protocol can be used to identify natural refolding intermediates, the complex conformations of these intermediates, including the way the TMHs realign in a zigzag-like manner, cannot be directly determined.

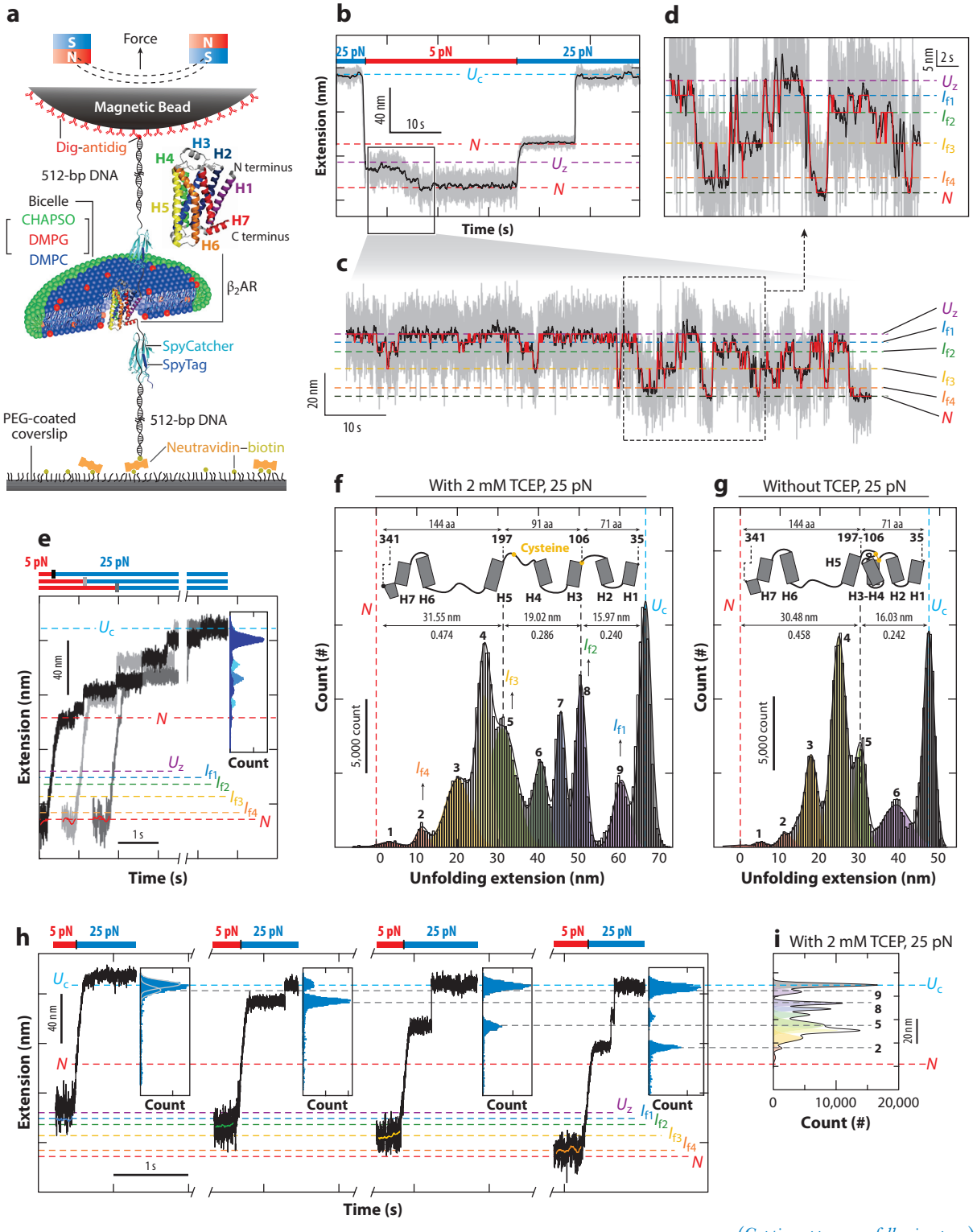

(Caption appears on following page)

Figure 5 (*Figure appears on preceding page*)

(*a*) Schematic of the magnetic tweezer-based folding experiments on human β_2AR. (*b*) The mechanical cycle for the low-force refolding of β_2AR. (*c*,*d*) Representative folding traces. State locations and intermediate form transitions were identified using hidden Markov modeling. (*e*) Force-jump experiments for the high-force unfolding of native-state β_2AR. (*f*,*g*) Extension distribution during high-force unfolding of native β_2AR after (*f*) disrupting or (*g*) preserving disulfide bonds. (*h*) Force-jump experiments for the high-force unfolding of intermediate-state β_2AR. (*i*) Extension distribution (replicate of panel *f*) rotated and aligned with the extension histograms in panel *h*. Abbreviations: β_2AR, β_2 adrenergic receptor; CHAPSO, 3-([3-cholamidopropyl]dimethylammonio)-2-hydroxy-1-propanesulfonate; DMPC, dimyristoyl phosphatidylcholine; DMPG, dimyristoyl phosphatidylglycerol; PEG, polyethylene glycol; TCEP, tris(2-carboxyethyl)phosphine; U_c, unstructured state. Figure reproduced with permission from Reference 73.

Next, a stronger force unfolding protocol can be used to permit all of the extension values reflected by the magnetic bead to be collected until the U_c state is achieved. In the resulting stronger force unfolding data, the distance between unfolding peaks translates directly into the number of amino acids that have unfolded (**Figure 5*e*,*f***). Furthermore, by introducing disulfide bonds at known locations, the unfolding process can be further explored while the unfolding of certain parts of the structure is blocked. For example, in the case of human β_2 adrenergic receptor (β_2AR), preservation of a conserved disulfide bond, by leaving out a reducing agent, led to the selective disappearance of the unfolding data between the fifth and eighth peaks, indicating that the part that disappeared corresponds to the unfolding of the amino acids knotted by the disulfide bond (**Figure 5*f*,*g***). In addition, the ratio of the unfolding extensions spanned by the first five peaks (peaks 1 to 5) and the last two peaks (peaks 8 to U_c) virtually exactly matches the ratio of the number of amino acids placed C terminal (144 amino acids, in this case) and N terminal (71 amino acids) to the disulfide bond (**Figure 5*f***). These observations collectively point to strictly one-directional unfolding of human β_2AR from the C to the N terminus (and thus, one-directional folding from the N to the C terminus). By applying force jumps during the refolding process at low force levels, a one-to-one relationship can be established between the low-force refolding and high-force unfolding intermediates (**Figure 5*h*,*i***).

This suggests a streamlining of magnetic tweezers experiments in which native refolding intermediates are first identified under low piconewton-scale tension. Structural states are then inferred from high-force unfolding data, and this structural information can, in turn, be extrapolated back to the low-force refolding intermediates. By applying this method, Yoon and colleagues identified a hierarchical folding pathway that begins at the N terminus and works its way toward the C terminus of proteins for two evolutionary distant proteins, *E. coli* GlpG and human β_2AR (73).

5. CONCLUSION

With recent advances in the field, it is now clear that high-resolution single-molecule magnetic tweezers can track nanometer changes with a millisecond-scale or shorter resolution. The magnetic beads and tether that are used to deliver magnetic force to target single molecules largely dampen the faster dynamics of target molecules and act as a low-pass filter. At the same time, the bead–tether construct increases the measurement noise due to their Brownian breathing motions. We showed that the use of smaller magnetic beads and shorter submicrometer tethers can improve dynamic response time by decreasing viscous drag on the bead and increasing the stiffness of the tether. In addition, shorter tethers reduce the Brownian noise of the bead–tether construct, improving magnetic tweezer measurement precision. Because magnetic tweezers should generate forces between 1 and 100 pN to modulate biological structures and their interactions, adoption of smaller magnetic beads requires the beads themselves to exhibit much higher mass saturation magnetization.

High-resolution magnetic tweezers have been used recently to explore the conformational transitions that play critical roles in mechanotransduction in cell signaling circuits, protein biogenesis, and homeostasis. In particular, the force-clamping capacity of magnetic tweezers has enabled many unique observations at near-equilibrium conditions. Considering the relative ease with which groups can assemble a high-resolution magnetic tweezer setup and the general availability of the software for running it, we anticipate that more and more biochemists and biologists will adopt single-molecule force spectroscopy in their own research.

Moreover, as recent advances in cryo-EM have facilitated the experimental determination of the tertiary and quaternary structures of proteins and protein complexes with unprecedented speed, the number of situations in which the magnetic tweezer technique has proven useful has only increased. Since it is possible to explore the mechanical responses of target proteins—including unfolding and refolding—using protein tags (e.g., HaloTag and SpyTag) delivered to specific sites in the target protein's structure, all of these new cryo-EM structures will guide both the selection of tagging sites and the interpretation of single-molecule force spectroscopy signals. The new computational platforms that permit direct structural predictions from sequence information alone will also facilitate the design and analysis of magnetic tweezer experiments (155, 156). At the same time, many, if not all, cryo-EM structures are obtained from freely floating (but snap-frozen) samples and thus represent the states of target proteins under zero mechanical tension. Magnetic tweezers, and more generally, all single-molecule force spectroscopy tools, have the unique potential to reveal the structural changes induced by mechanical tension. This capacity will permit us to expand our understanding of how the atomic structures revealed by cryo-EM respond and adapt to mechanical cues. Thus, the coming decades will be exciting as more groups use single-molecule magnetic tweezers to make many interesting discoveries.

DISCLOSURE STATEMENT

The authors are not aware of any affiliations, memberships, funding, or financial holdings that might be perceived as affecting the objectivity of this review.

ACKNOWLEDGMENTS

This work was supported by the National Research Foundation of Korea funded by the Korean government (the Ministry of Science and Information and Communications Technology) (grant 2021R1A3B1071354 to T.-Y.Y.).

LITERATURE CITED

1. Freundlich H, Seifriz W. 1923. Über die Elastizität von Solen und Gelen. *Z. Phys. Chem.* 104U:233–61
2. Crick FHC, Hughes AFW. 1950. The physical properties of cytoplasm. *Exp. Cell Res.* 1:37–80
3. Smith SB, Finzi L, Bustamante C. 1992. Direct mechanical measurements of the elasticity of single DNA molecules by using magnetic beads. *Science* 258:1122–26
4. Strick TR, Allemand JF, Bensimon D, Bensimon A, Croquette V. 1996. The elasticity of a single supercoiled DNA molecule. *Science* 271:1835–37
5. Haber C, Wirtz D. 2000. Magnetic tweezers for DNA micromanipulation. *Rev. Sci. Instrum.* 71:4561–70
6. Gosse C, Croquette V. 2002. Magnetic tweezers: micromanipulation and force measurement at the molecular level. *Biophys. J.* 82:3314–29
7. De Vlaminck I, Dekker C. 2012. Recent advances in magnetic tweezers. *Annu. Rev. Biophys.* 41:453–72
8. Block SM, Goldstein LS, Schnapp BJ. 1990. Bead movement by single kinesin molecules studied with optical tweezers. *Nature* 348:348–52
9. Svoboda K, Schmidt CF, Schnapp BJ, Block SM. 1993. Direct observation of kinesin stepping by optical trapping interferometry. *Nature* 365:721–27

10. Smith SB, Cui Y, Bustamante C. 1996. Overstretching B-DNA: the elastic response of individual double-stranded and single-stranded DNA molecules. *Science* 271:795–99
11. Simmons RM, Finer JT, Chu S, Spudich JA. 1996. Quantitative measurements of force and displacement using an optical trap. *Biophys. J.* 70:1813–22
12. Moffitt JR, Chemla YR, Smith SB, Bustamante C. 2008. Recent advances in optical tweezers. *Annu. Rev. Biochem.* 77:205–28
13. Florin E-L, Moy VT, Gaub HE. 1994. Adhesion forces between individual ligand-receptor pairs. *Science* 264:415–17
14. Rief M, Gautel M, Oesterhelt F, Fernandez JM, Gaub HE. 1997. Reversible unfolding of individual titin immunoglobulin domains by AFM. *Science* 276:1109–12
15. Oberhauser AF, Marszalek PE, Erickson HP, Fernandez JM. 1998. The molecular elasticity of the extracellular matrix protein tenascin. *Nature* 393:181–85
16. Oesterhelt F, Oesterhelt D, Pfeiffer M, Engel A, Gaub HE, Muller DJ. 2000. Unfolding pathways of individual bacteriorhodopsins. *Science* 288:143–46
17. Neuman KC, Nagy A. 2008. Single-molecule force spectroscopy: optical tweezers, magnetic tweezers and atomic force microscopy. *Nat. Methods* 5:491–505
18. Wang MD, Yin H, Landick R, Gelles J, Block SM. 1997. Stretching DNA with optical tweezers. *Biophys. J.* 72:1335–46
19. Strick TR, Allemand JF, Bensimon D, Croquette V. 1998. Behavior of supercoiled DNA. *Biophys. J.* 74:2016–28
20. Liphardt J, Onoa B, Smith SB, Tinoco I Jr., Bustamante C. 2001. Reversible unfolding of single RNA molecules by mechanical force. *Science* 292:733–37
21. Abels J, Moreno-Herrero F, Van der Heijden T, Dekker C, Dekker NH. 2005. Single-molecule measurements of the persistence length of double-stranded RNA. *Biophys. J.* 88:2737–44
22. Koster DA, Croquette V, Dekker C, Shuman S, Dekker NH. 2005. Friction and torque govern the relaxation of DNA supercoils by eukaryotic topoisomerase IB. *Nature* 434:671–74
23. Lee G, Abdi K, Jiang Y, Michaely P, Bennett V, Marszalek PE. 2006. Nanospring behaviour of ankyrin repeats. *Nature* 440:246–49
24. Kishino A, Yanagida T. 1988. Force measurements by micromanipulation of a single actin filament by glass needles. *Nature* 334:74–76
25. Smith DE, Tans SJ, Smith SB, Grimes S, Anderson DL, Bustamante C. 2001. The bacteriophage φ29 portal motor can package DNA against a large internal force. *Nature* 413:748–52
26. Asbury CL, Fehr AN, Block SM. 2003. Kinesin moves by an asymmetric hand-over-hand mechanism. *Science* 302:2130–34
27. Abbondanzieri EA, Greenleaf WJ, Shaevitz JW, Landick R, Block SM. 2005. Direct observation of base-pair stepping by RNA polymerase. *Nature* 438:460–65
28. Wen J-D, Lancaster L, Hodges C, Zeri A-C, Yoshimura SH, et al. 2008. Following translation by single ribosomes one codon at a time. *Nature* 452:598–603
29. Kellermayer MS, Smith SB, Granzier HL, Bustamante C. 1997. Folding-unfolding transitions in single titin molecules characterized with laser tweezers. *Science* 276:1112–16
30. Marszalek PE, Lu H, Li H, Carrion-Vazquez M, Oberhauser AF, et al. 1999. Mechanical unfolding intermediates in titin modules. *Nature* 402:100–3
31. Woodside MT, Block SM. 2014. Reconstructing folding energy landscapes by single-molecule force spectroscopy. *Annu. Rev. Biophys.* 43:19–39
32. Neupane K, Foster DA, Dee DR, Yu H, Wang F, Woodside MT. 2016. Direct observation of transition paths during the folding of proteins and nucleic acids. *Science* 352:239–42
33. Yu H, Siewny MG, Edwards DT, Sanders AW, Perkins TT. 2017. Hidden dynamics in the unfolding of individual bacteriorhodopsin proteins. *Science* 355:945–50
34. Bustamante C, Alexander L, Maciuba K, Kaiser CM. 2020. Single-molecule studies of protein folding with optical tweezers. *Annu. Rev. Biochem.* 89:443–70
35. Danilowicz C, Greenfield D, Prentiss M. 2005. Dissociation of ligand–receptor complexes using magnetic tweezers. *Anal. Chem.* 77:3023–28

36. Kim J, Zhang C-Z, Zhang X, Springer TA. 2010. A mechanically stabilized receptor–ligand flex-bond important in the vasculature. *Nature* 466:992–95
37. Kostrz D, Wayment-Steele HK, Wang JL, Follenfant M, Pande VS, et al. 2019. A modular DNA scaffold to study protein–protein interactions at single-molecule resolution. *Nat. Nanotechnol.* 14:988–93
38. del Rio A, Perez-Jimenez R, Liu R, Roca-Cusachs P, Fernandez JM, Sheetz MP. 2009. Stretching single talin rod molecules activates vinculin binding. *Science* 323:638–41
39. Yao M, Qiu W, Liu R, Efremov AK, Cong P, et al. 2014. Force-dependent conformational switch of α-catenin controls vinculin binding. *Nat. Commun.* 5:4525
40. Buckley CD, Tan J, Anderson KL, Hanein D, Volkmann N, et al. 2014. The minimal cadherin-catenin complex binds to actin filaments under force. *Science* 346:1254211
41. Seo D, Southard KM, Kim JW, Lee HJ, Farlow J, et al. 2016. A mechanogenetic toolkit for interrogating cell signaling in space and time. *Cell* 165:1507–18
42. Harris AR, Jreij P, Fletcher DA. 2018. Mechanotransduction by the actin cytoskeleton: converting mechanical stimuli into biochemical signals. *Annu. Rev. Biophys.* 47:617–31
43. Ashkin A, Dziedzic JM, Bjorkholm JE, Chu S. 1986. Observation of a single-beam gradient force optical trap for dielectric particles. *Opt. Lett.* 11:288–90
44. Shaevitz JW, Abbondanzieri EA, Landick R, Block SM. 2003. Backtracking by single RNA polymerase molecules observed at near-base-pair resolution. *Nature* 426:684–87
45. Peterman EJ, Gittes F, Schmidt CF. 2003. Laser-induced heating in optical traps. *Biophys. J.* 84:1308–16
46. Čižmár T, Mazilu M, Dholakia K. 2010. In situ wavefront correction and its application to micromanipulation. *Nat. Photon.* 4:388–94
47. Park J-H, Yu Z, Lee K, Lai P, Park Y. 2018. Wavefront shaping techniques for controlling multiple light scattering in biological tissues: toward *in vivo* applications. *APL Photon*. 3:100901
48. Favre-Bulle IA, Stilgoe AB, Scott EK, Rubinsztein-Dunlop H. 2019. Optical trapping in vivo: theory, practice, and applications. *Nanophotonics* 8:1023–40
49. Hughes ML, Dougan L. 2016. The physics of pulling polyproteins: a review of single molecule force spectroscopy using the AFM to study protein unfolding. *Rep. Prog. Phys.* 79:076601
50. Edwards DT, Faulk JK, Sanders AW, Bull MS, Walder R, et al. 2015. Optimizing 1-μs-resolution single-molecule force spectroscopy on a commercial atomic force microscope. *Nano Lett*. 15:7091–98
51. Churnside AB, Sullan RM, Nguyen DM, Case SO, Bull MS, et al. 2012. Routine and timely sub-picoNewton force stability and precision for biological applications of atomic force microscopy. *Nano Lett*. 12:3557–61
52. Edwards DT, Faulk JK, LeBlanc MA, Perkins TT. 2017. Force spectroscopy with 9-μs resolution and sub-pN stability by tailoring AFM cantilever geometry. *Biophys. J.* 113:2595–600
53. Edwards DT, LeBlanc MA, Perkins TT. 2021. Modulation of a protein-folding landscape revealed by AFM-based force spectroscopy notwithstanding instrumental limitations. *PNAS* 118:e2015728118
54. Vilfan ID, Lipfert J, Koster D, Lemay S, Dekker N. 2009. Magnetic tweezers for single-molecule experiments. In *Handbook of Single-Molecule Biophysics*, ed. P Hinterdorfer, A Oijen, pp. 371–95. New York: Springer
55. Lipfert J, Hao X, Dekker NH. 2009. Quantitative modeling and optimization of magnetic tweezers. *Biophys. J.* 96:5040–49
56. te Velthuis AJ, Kerssemakers JW, Lipfert J, Dekker NH. 2010. Quantitative guidelines for force calibration through spectral analysis of magnetic tweezers data. *Biophys. J.* 99:1292–302
57. Lansdorp BM, Tabrizi SJ, Dittmore A, Saleh OA. 2013. A high-speed magnetic tweezer beyond 10,000 frames per second. *Rev. Sci. Instrum.* 84:044301
58. Dulin D, Cui TJ, Cnossen J, Docter MW, Lipfert J, Dekker NH. 2015. High spatiotemporal-resolution magnetic tweezers: calibration and applications for DNA dynamics. *Biophys. J.* 109:2113–25
59. Huhle A, Klaue D, Brutzer H, Daldrop P, Joo S, et al. 2015. Camera-based three-dimensional real-time particle tracking at kHz rates and Ångström accuracy. *Nat. Commun.* 6:5885
60. Kirby TJ, Lammerding J. 2018. Emerging views of the nucleus as a cellular mechanosensor. *Nat. Cell Biol.* 20:373–81
61. Romani P, Valcarcel-Jimenez L, Frezza C, Dupont S. 2021. Crosstalk between mechanotransduction and metabolism. *Nat. Rev. Mol. Cell Biol.* 22:22–38

62. Purcell EM. 1977. Life at low Reynolds number. *Am. J. Phys.* 45:3–11
63. Dill KA, Ghosh K, Schmit JD. 2011. Physical limits of cells and proteomes. *PNAS* 108:17876–82
64. Sawle L, Ghosh K. 2011. How do thermophilic proteins and proteomes withstand high temperature? *Biophys. J.* 101:217–27
65. Woodside MT, Behnke-Parks WM, Larizadeh K, Travers K, Herschlag D, Block SM. 2006. Nanomechanical measurements of the sequence-dependent folding landscapes of single nucleic acid hairpins. *PNAS* 103:6190–95
66. Krebs MD, Erb RM, Yellen BB, Samanta B, Bajaj A, et al. 2009. Formation of ordered cellular structures in suspension via label-free negative magnetophoresis. *Nano Lett.* 9:1812–17
67. Kose AR, Fischer B, Mao L, Koser H. 2009. Label-free cellular manipulation and sorting via biocompatible ferrofluids. *PNAS* 106:21478–83
68. Zeng J, Deng YX, Vedantam P, Tzeng TR, Xuan XC. 2013. Magnetic separation of particles and cells in ferrofluid flow through a straight microchannel using two offset magnets. *J. Magn. Magn. Mater.* 346:118–23
69. Furlani EP. 2006. Analysis of particle transport in a magnetophoretic microsystem. *J. Appl. Phys.* 99:024912
70. Timonen JVI, Grzybowski BA. 2017. Tweezing of magnetic and non-magnetic objects with magnetic fields. *Adv. Mater.* 29:1603516
71. Chen H, Fu H, Zhu X, Cong P, Nakamura F, Yan J. 2011. Improved high-force magnetic tweezers for stretching and refolding of proteins and short DNA. *Biophys. J.* 100:517–23
72. Liu R, Garcia-Manyes S, Sarkar A, Badilla CL, Fernandez JM. 2009. Mechanical characterization of protein L in the low-force regime by electromagnetic tweezers/evanescent nanometry. *Biophys. J.* 96:3810–21
73. Choi HK, Min D, Kang H, Shon MJ, Rah SH, et al. 2019. Watching helical membrane proteins fold reveals a common N-to-C-terminal folding pathway. *Science* 366:1150–56
74. Fonnum G, Johansson C, Molteberg A, Morup S, Aksnes E. 2005. Characterisation of Dynabeads® by magnetization measurements and Mossbauer spectroscopy. *J. Magn. Magn. Mater.* 293:41–47
75. De Vlaminck I, Henighan T, van Loenhout MT, Burnham DR, Dekker C. 2012. Magnetic forces and DNA mechanics in multiplexed magnetic tweezers. *PLOS ONE* 7:e41432
76. van Oene MM, Dickinson LE, Pedaci F, Kober M, Dulin D, et al. 2015. Biological magnetometry: torque on superparamagnetic beads in magnetic fields. *Phys. Rev. Lett.* 114:218301
77. Yan J, Skoko D, Marko JF. 2004. Near-field-magnetic-tweezer manipulation of single DNA molecules. *Phys. Rev. E Stat. Nonlin. Soft. Matter Phys.* 70:011905
78. Ribeck N, Saleh OA. 2008. Multiplexed single-molecule measurements with magnetic tweezers. *Rev. Sci. Instrum.* 79:094301
79. Tapia-Rojo R, Eckels EC, Fernandez JM. 2019. Ephemeral states in protein folding under force captured with a magnetic tweezers design. *PNAS* 116:7873–78
80. Lansdorp BM, Saleh OA. 2012. Power spectrum and Allan variance methods for calibrating single-molecule video-tracking instruments. *Rev. Sci. Instrum.* 83:025115
81. Yu Z, Dulin D, Cnossen J, Kober M, van Oene MM, et al. 2014. A force calibration standard for magnetic tweezers. *Rev. Sci. Instrum.* 85:123114
82. Daldrop P, Brutzer H, Huhle A, Kauert DJ, Seidel R. 2015. Extending the range for force calibration in magnetic tweezers. *Biophys. J.* 108:2550–61
83. Barbic M, Mock JJ, Gray AP, Schultz S. 2001. Scanning probe electromagnetic tweezers. *Appl. Phys. Lett.* 79:1897–99
84. Jiang C, Lionberger TA, Wiener DM, Meyhofer E. 2016. Electromagnetic tweezers with independent force and torque control. *Rev. Sci. Instrum.* 87:084304
85. Matthews BD, LaVan DA, Overby DR, Karavitis J, Ingber DE. 2004. Electromagnetic needles with submicron pole tip radii for nanomanipulation of biomolecules and living cells. *Appl. Phys. Lett.* 85:2968–70
86. Chiou C-H, Lee G-B. 2005. A micromachined DNA manipulation platform for the stretching and rotation of a single DNA molecule. *J. Micromech. Microeng.* 15:109–17

87. Chiou CH, Huang YY, Chiang MH, Lee HH, Lee GB. 2006. New magnetic tweezers for investigation of the mechanical properties of single DNA molecules. *Nanotechnology* 17:1217–24
88. Wang X, Ho C, Tsatskis Y, Law J, Zhang Z, et al. 2019. Intracellular manipulation and measurement with multipole magnetic tweezers. *Sci. Robot.* 4:eaav6180
89. Kim JW, Jeong HK, Southard KM, Jun YW, Cheon J. 2018. Magnetic nanotweezers for interrogating biological processes in space and time. *Acc. Chem. Res.* 51:839–49
90. Greenleaf WJ, Woodside MT, Abbondanzieri EA, Block SM. 2005. Passive all-optical force clamp for high-resolution laser trapping. *Phys. Rev. Lett.* 95:208102
91. Romano G, Sacconi L, Capitanio M, Pavone FS. 2003. Force and torque measurements using magnetic micro beads for single molecule biophysics. *Opt. Commun.* 215:323–31
92. Lee JU, Shin W, Lim Y, Kim J, Kim WR, et al. 2021. Non-contact long-range magnetic stimulation of mechanosensitive ion channels in freely moving animals. *Nat. Mater.* 20:1029–36
93. van Reenen A, Gutierrez-Mejia F, van IJzendoorn LJ, Prins MWJ. 2013. Torsion profiling of proteins using magnetic particles. *Biophys. J.* 104:1073–80
94. Maier B, Bensimon D, Croquette V. 2000. Replication by a single DNA polymerase of a stretched single-stranded DNA. *PNAS* 97:12002–7
95. Manosas M, Xi XG, Bensimon D, Croquette V. 2010. Active and passive mechanisms of helicases. *Nucleic Acids Res.* 38:5518–26
96. Dekker NH, Rybenkov VV, Duguet M, Crisona NJ, Cozzarelli NR, et al. 2002. The mechanism of type IA topoisomerases. *PNAS* 99:12126–31
97. Crut A, Koster DA, Seidel R, Wiggins CH, Dekker NH. 2007. Fast dynamics of supercoiled DNA revealed by single-molecule experiments. *PNAS* 104:11957–62
98. Bell GI. 1978. Models for the specific adhesion of cells to cells. *Science* 200:618–27
99. Evans E, Ritchie K. 1997. Dynamic strength of molecular adhesion bonds. *Biophys. J.* 72:1541–55
100. Dudko OK, Hummer G, Szabo A. 2008. Theory, analysis, and interpretation of single-molecule force spectroscopy experiments. *PNAS* 105:15755–60
101. Lof A, Walker PU, Sedlak SM, Gruber S, Obser T, et al. 2019. Multiplexed protein force spectroscopy reveals equilibrium protein folding dynamics and the low-force response of von Willebrand factor. *PNAS* 116:18798–807
102. Chen H, Yuan G, Winardhi RS, Yao M, Popa I, et al. 2015. Dynamics of equilibrium folding and unfolding transitions of titin immunoglobulin domain under constant forces. *J. Am. Chem. Soc.* 137:3540–46
103. Neuman KC, Lionnet T, Allemand JF. 2007. Single-molecule micromanipulation techniques. *Annu. Rev. Mater. Res.* 37:33–67
104. Bouchiat C, Wang MD, Allemand J, Strick T, Block SM, Croquette V. 1999. Estimating the persistence length of a worm-like chain molecule from force-extension measurements. *Biophys. J.* 76:409–13
105. Schaffer E, Norrelykke SF, Howard J. 2007. Surface forces and drag coefficients of microspheres near a plane surface measured with optical tweezers. *Langmuir* 23:3654–65
106. Wong WP, Halvorsen K. 2006. The effect of integration time on fluctuation measurements: calibrating an optical trap in the presence of motion blur. *Opt. Express* 14:12517–31
107. Ostrofet E, Papini FS, Dulin D. 2018. Correction-free force calibration for magnetic tweezers experiments. *Sci. Rep.* 8:15920
108. Klaue D, Seidel R. 2009. Torsional stiffness of single superparamagnetic microspheres in an external magnetic field. *Phys. Rev. Lett.* 102:028302
109. Otto O, Gutsche C, Kremer F, Keyser UF. 2008. Optical tweezers with 2.5 kHz bandwidth video detection for single-colloid electrophoresis. *Rev. Sci. Instrum.* 79:023710
110. Gibson GM, Leach J, Keen S, Wright AJ, Padgett MJ. 2008. Measuring the accuracy of particle position and force in optical tweezers using high-speed video microscopy. *Opt. Express* 16:14561–70
111. Otto O, Czerwinski F, Gornall JL, Stober G, Oddershede LB, et al. 2010. Real-time particle tracking at 10,000 fps using optical fiber illumination. *Opt. Express* 18:22722–33
112. El-Desouki M, Deen MJ, Fang Q, Liu L, Tse F, Armstrong D. 2009. CMOS image sensors for high speed applications. *Sensors* 9:430–44
113. Shon MJ, Rah SH, Yoon TY. 2019. Submicrometer elasticity of double-stranded DNA revealed by precision force-extension measurements with magnetic tweezers. *Sci. Adv.* 5:eaav1697

114. Dulin D, Barland S, Hachair X, Pedaci F. 2014. Efficient illumination for microsecond tracking microscopy. *PLOS ONE* 9:e107335
115. Cnossen JP, Dulin D, Dekker NH. 2014. An optimized software framework for real-time, high-throughput tracking of spherical beads. *Rev. Sci. Instrum.* 85:103712
116. De Vlaminck I, Henighan T, van Loenhout MT, Pfeiffer I, Huijts J, et al. 2011. Highly parallel magnetic tweezers by targeted DNA tethering. *Nano Lett.* 11:5489–93
117. Allan DW. 1966. Statistics of atomic frequency standards. *Proc. IEEE* 54:221–30
118. Czerwinski F, Richardson AC, Oddershede LB. 2009. Quantifying noise in optical tweezers by Allan variance. *Opt. Express* 17:13255–69
119. Rico F, Gonzalez L, Casuso I, Puig-Vidal M, Scheuring S. 2013. High-speed force spectroscopy unfolds titin at the velocity of molecular dynamics simulations. *Science* 342:741–43
120. Seol Y, Li J, Nelson PC, Perkins TT, Betterton MD. 2007. Elasticity of short DNA molecules: theory and experiment for contour lengths of 0.6–7 μm. *Biophys. J.* 93:4360–73
121. Shon MJ, Kim H, Yoon TY. 2018. Focused clamping of a single neuronal SNARE complex by complexin under high mechanical tension. *Nat. Commun.* 9:3639
122. Kim C, Shon MJ, Kim SH, Eun GS, Ryu JK, et al. 2021. Extreme parsimony in ATP consumption by 20S complexes in the global disassembly of single SNARE complexes. *Nat. Commun.* 12:3206
123. Janissen R, Berghuis BA, Dulin D, Wink M, van Laar T, Dekker NH. 2014. Invincible DNA tethers: covalent DNA anchoring for enhanced temporal and force stability in magnetic tweezers experiments. *Nucleic Acids Res.* 42:e137
124. Dietz H, Berkemeier F, Bertz M, Rief M. 2006. Anisotropic deformation response of single protein molecules. *PNAS* 103:12724–28
125. van Noort SJ, van der Werf KO, Eker AP, Wyman C, de Grooth BG, et al. 1998. Direct visualization of dynamic protein-DNA interactions with a dedicated atomic force microscope. *Biophys. J.* 74:2840–49
126. Synakewicz M, Bauer D, Rief M, Itzhaki LS. 2019. Bioorthogonal protein-DNA conjugation methods for force spectroscopy. *Sci. Rep.* 9:13820
127. England CG, Luo H, Cai W. 2015. HaloTag technology: a versatile platform for biomedical applications. *Bioconjug. Chem.* 26:975–86
128. Popa I, Rivas-Pardo JA, Eckels EC, Echelman DJ, Badilla CL, et al. 2016. A HaloTag anchored ruler for week-long studies of protein dynamics. *J. Am. Chem. Soc.* 138:10546–53
129. Rivas-Pardo JA, Eckels EC, Popa I, Kosuri P, Linke WA, Fernandez JM. 2016. Work done by titin protein folding assists muscle contraction. *Cell Rep.* 14:1339–47
130. Tapia-Rojo R, Alonso-Caballero A, Fernandez JM. 2020. Talin folding as the tuning fork of cellular mechanotransduction. *PNAS* 117:21346–53
131. Tapia-Rojo R, Alonso-Caballero A, Fernandez JM. 2020. Direct observation of a coil-to-helix contraction triggered by vinculin binding to talin. *Sci. Adv.* 6:eaaz4707
132. Spadaro D, Le S, Laroche T, Mean I, Jond L, et al. 2017. Tension-dependent stretching activates ZO-1 to control the junctional localization of its interactors. *Curr. Biol.* 27:3783–95.e8
133. Le S, Hu X, Yao M, Chen H, Yu M, et al. 2017. Mechanotransmission and mechanosensing of human alpha-actinin 1. *Cell Rep.* 21:2714–23
134. Yu M, Zhao Z, Chen Z, Le S, Yan J. 2020. Modulating mechanical stability of heterodimerization between engineered orthogonal helical domains. *Nat. Commun.* 11:4476
135. Zakeri B, Fierer JO, Celik E, Chittock EC, Schwarz-Linek U, et al. 2012. Peptide tag forming a rapid covalent bond to a protein, through engineering a bacterial adhesin. *PNAS* 109:E690–97
136. Min D, Arbing MA, Jefferson RE, Bowie JU. 2016. A simple DNA handle attachment method for single molecule mechanical manipulation experiments. *Protein Sci.* 25:1535–44
137. Kriegel F, Ermann N, Lipfert J. 2017. Probing the mechanical properties, conformational changes, and interactions of nucleic acids with magnetic tweezers. *J. Struct. Biol.* 197:26–36
138. Shi Z, Graber ZT, Baumgart T, Stone HA, Cohen AE. 2018. Cell membranes resist flow. *Cell* 175:1769–79.e13
139. Linke WA. 2018. Titin gene and protein functions in passive and active muscle. *Annu. Rev. Physiol.* 80:389–411

140. Leake MC, Wilson D, Gautel M, Simmons RM. 2004. The elasticity of single titin molecules using a two-bead optical tweezers assay. *Biophys. J.* 87:1112–35
141. Eckels EC, Tapia-Rojo R, Rivas-Pardo JA, Fernández JM. 2018. The work of titin protein folding as a major driver in muscle contraction. *Annu. Rev. Physiol.* 80:327–51
142. Parsons JT, Horwitz AR, Schwartz MA. 2010. Cell adhesion: integrating cytoskeletal dynamics and cellular tension. *Nat. Rev. Mol. Cell Biol.* 11:633–43
143. Yu M, Yuan X, Lu C, Le S, Kawamura R, et al. 2017. mDia1 senses both force and torque during F-actin filament polymerization. *Nat. Commun.* 8:1650
144. Le S, Yu M, Hovan L, Zhao Z, Ervasti J, et al. 2018. Dystrophin as a molecular shock absorber. *ACS Nano* 12:12140–48
145. Plaxco KW, Dobson CM. 1996. Time-resolved biophysical methods in the study of protein folding. *Curr. Opin. Struct. Biol.* 6:630–36
146. Feng H, Vu ND, Zhou Z, Bai Y. 2004. Structural examination of Φ-value analysis in protein folding. *Biochemistry* 43:14325–31
147. Oesterhelt F, Oesterhelt D, Pfeiffer M, Engel A, Gaub HE, Müller DJ. 2000. Unfolding pathways of individual bacteriorhodopsins. *Science* 288:143–46
148. Hoffmann A, Neupane K, Woodside MT. 2013. Single-molecule assays for investigating protein misfolding and aggregation. *Phys. Chem. Chem. Phys.* 15:7934–48
149. Guttula D, Yao M, Baker K, Yang L, Goult BT, et al. 2019. Calcium-mediated protein folding and stabilization of *Salmonella* biofilm-associated protein A. *J. Mol. Biol.* 431:433–43
150. Haldar S, Tapia-Rojo R, Eckels EC, Valle-Orero J, Fernandez JM. 2017. Trigger factor chaperone acts as a mechanical foldase. *Nat. Commun.* 8:668
151. Cheng Y. 2018. Membrane protein structural biology in the era of single particle cryo-EM. *Curr. Opin. Struct. Biol.* 52:58–63
152. Quistgaard EM, Low C, Guettou F, Nordlund P. 2016. Understanding transport by the major facilitator superfamily (MFS): structures pave the way. *Nat. Rev. Mol. Cell Biol.* 17:123–32
153. Locher KP. 2016. Mechanistic diversity in ATP-binding cassette (ABC) transporters. *Nat. Struct. Mol. Biol.* 23:487–93
154. Guna A, Hegde RS. 2018. Transmembrane domain recognition during membrane protein biogenesis and quality control. *Curr. Biol.* 28:R498–511
155. Jumper J, Evans R, Pritzel A, Green T, Figurnov M, et al. 2021. Highly accurate protein structure prediction with AlphaFold. *Nature* 596:583–89
156. Baek M, DiMaio F, Anishchenko I, Dauparas J, Ovchinnikov S, et al. 2021. Accurate prediction of protein structures and interactions using a three-track neural network. *Science* 373:871–76